Journal of Catalysis 374 (2019) 143–149

Contents lists available at ScienceDirect

Journal of Catalysis

journal homepage: www.elsevier.com/locate/jcat

Tunable catalytic activity of cobalt-intercalated layered MnO_2 for water oxidation through confinement and local ordering

Jinliang Ning [a], James W. Furness [a], Yubo Zhang [a], Akila C. Thenuwara [b], Richard C. Remsing [b,c], Michael L. Klein [b,c,d], Daniel R. Strongin [b], Jianwei Sun [a,*]

[a] Department of Physics and Engineering Physics, Tulane University, New Orleans, LA 70118, USA
[b] Department of Chemistry, Temple University, Philadelphia, PA 19122, USA
[c] Institute for Computational Molecular Science, Temple University, Philadelphia, PA 19122, USA
[d] Department of Physics, Temple University, Philadelphia, PA 19122, USA

ARTICLE INFO

Article history:
Received 4 September 2018
Revised 22 April 2019
Accepted 22 April 2019

Keywords:
Layered materials
Atomic intercalation
Oxygen evolution reaction
Density functional theory

ABSTRACT

The lowering of reaction overpotentials is a persistent and universal goal in the development of catalysts for (photo)electrochemistry, which can usually be facilitated by selectively stabilizing one reaction intermediate over another. In this mechanistic study of the oxygen evolution reaction (OER) catalyzed by cobalt-intercalated layered MnO_2, we show that confinement effects and local cobalt atomic ordering in the interlayer space can be synergistically used to tune the adsorption energies of O, OH, and OOH reaction intermediates and the scaling relationship between them. In general, the interlayer confinement destabilizes the adsorption of intermediates for the OER, but clustering Co atoms can selectively stabilize the adsorption of OOH in particular. After considering both effects, our model predicts an overpotential of 0.30 V for the Co-intercalated MnO_2 catalyzed OER, in excellent agreement with the experimental result of 0.36 V. These new insights explain the enhanced catalytic performance of MnO_2 by intercalating atoms and illuminate a route for engineering non-toxic precious-metal-free catalysts through designed layered materials.

1. Introduction

The conversion of solar energy into chemical fuels is a promising way to transition from the current unsustainable use of fossil fuels towards a sustainable economy [1–3] of hydrogen-based fuels. A key step towards this goal is the efficient and economical splitting of water into H_2 and O_2 [4–6]. Water splitting involves two half reactions, the hydrogen evolution reaction (HER) and the oxygen evolution reaction (OER), the latter of which is typically rate-determining and requires high-performance catalysts. Current high-performance OER catalysts often are comprised of precious metal oxides, such as RuO_2 and IrO_2 [7], whose prohibitive costs prevent their economic viability for commercial applications. Consequently, much effort is devoted to developing highly active OER catalysts from nonprecious elements, with transition metal oxides/hydroxides (especially Ni, Co, Fe, and Mn) [8–15], chalcogenides [16–18], phosphates [19–22], and perovskites [23] showing considerable promise. Among the potential candidates is birnessite, an earth-abundant non-toxic layered mineral composed of edge-sharing MnO_6 octahedra and an interlayer of hydrated cations with a general formula $AMn_4O_8{\cdot}3H_2O$ (A = alkali and alkaline earth metals e.g. K, Na, Ca) [24–27]. The structural motif of birnessite shows a similarity to the oxygen evolution centre Mn_4CaO_5 cubane configuration of photosystem II (PS II) [28–30], nature's own choice for water splitting and solar energy harvesting. Although birnessite exhibits only moderate activity towards the electrocatalytic OER reaction, multiple engineering techniques are available to improve its performance [31–36]. By intercalating birnessite with cobalt ions, an excellent catalytic performance with the overpotential of 0.36 eV has been reported [35].

Despite the progress made in birnessite OER catalyst design, a detailed understanding of the catalytic mechanism for the intercalated birnessite systems remains elusive and stands as a severe limitation to further development. First-principles calculations based on density functional theory (DFT) provide a powerful tool for investigating catalytic mechanisms, allowing both an explanation of experimental findings as well as a computational screening of candidate catalysts that is much more efficient than the traditional "trial and error" experimental approach. Pioneering first-principles work by Nørskov and collaborators [37,38] established the importance of scaling relationships between adsorption energies of different

* Corresponding author.
E-mail address: jsun@tulane.edu (J. Sun).

https://doi.org/10.1016/j.jcat.2019.04.037
0021-9517/

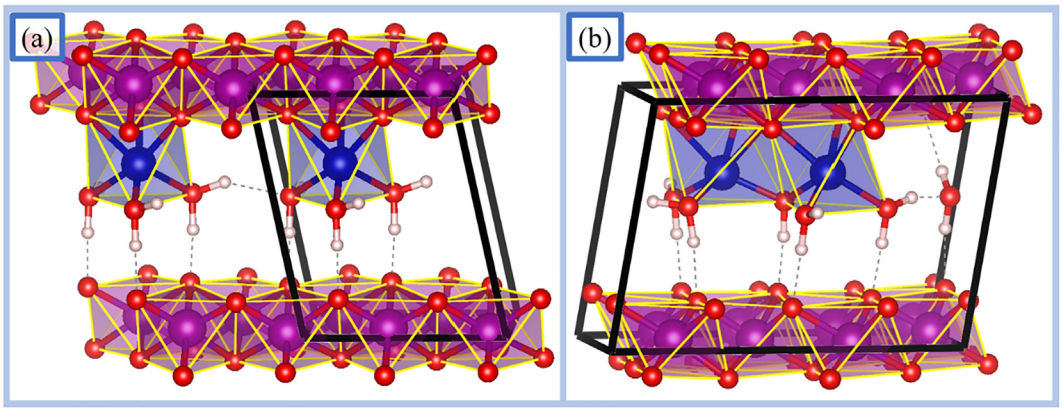

Fig. 1. The geometric models for the Co-intercalated layered MnO_2 without reaction intermediates for (a) InterL and (b) Co-pair models. Spectator atoms are identified as H (white), O (red), Co (blue), and Mn (purple). Unit cell used for calculations is indicated by a black box.

reaction intermediates in finding catalytic mechanisms and designing novel catalysts [39–42]. These scaling relationships result in a volcano-shaped curve of catalytic activity versus adsorption energy of a particular reaction intermediate, with activity improving towards the apex of the volcano [39–41]. However, the volcano's apex sets an upper bound on the catalytic activity [43–45]. Several strategies have been proposed to circumvent the scaling relationship by selectively stabilizing key reaction intermediates [46], achieved through the use of bifunctionality [47,48], promotors, ligands, electrolyte choice [49–51], engineering three-dimensional active sites at interfaces [52–54], and confined interlayer space [55]. In this work, we take the Co-intercalated layered MnO_2 birnessite as a prototypical case and show that layered materials with intercalated atoms facilitate intricate atomic interactions in the unique environment of the interlayer space. The atomic interactions within the interlayer enable a synergy of multiple selective stabilization mechanisms of key intermediates, and thus high tunability and improvement in catalytic performance for water oxidation.

2. Methods

2.1. Computational methods

In this work, we carry out density functional theory [56] calculations using the Vienna Ab-initio Simulation Package (VASP) [57] with the projector-augmented wave (PAW) method [58,59]. The recently developed strongly-constrained and appropriately-normed (SCAN) *meta*-GGA [60,61] is used for its superior performance in description of different chemical bonds and transition metal compounds [60–65]. A long range van der Waals correction is combined with SCAN through the rVV10 nonlocal correlation [66], a revised form of VV10, the Vydrov–Van Voorhis non-local correlation functional [67]. The PAW method is employed to treat the core ion-electron interaction and the valence configurations are taken as Mn: $3p^6 4s^1 3d^6$, O: $2s^2 2p^4$, Co: $3d^8 4s^1$ and H: $1s^1$. An energy cutoff of 520 eV is used to truncate the plane wave basis. We use Γ-centered meshes with a spacing threshold of 0.2 $Å^{-1}$ for K-space sampling. Geometries of the reaction models were allowed to relax until the maximum ionic forces were below a threshold of 0.02 eV $Å^{-1}$. Calculations for surface reactions employed a dipole moment correction, to correct for residual dipole moments perpendicular to the surface.

2.2. Model geometries

Two initial structures were employed to construct the intermediate models for study of the effect of confinement and local Co atom ordering of the Co intercalated layered birnessite, and the initial structures are illustrated in Fig. 1. The interlayer (InterL) model contains intercalated Co atoms that are well separated from each other. The basic InterL structural unit is similar to the triclinic phase of birnessite [24] and is shown in Fig. 1(a). This structure was chosen as a starting point for reaction modeling, with a general unit cell formula of $MMn_4O_8{\cdot}3H_2O$ (M = transition or alkali metal). In contrast to typical triclinic birnessite, the structural unit employed here places the interlayer atom (Co) at a position interacting with six O atoms, 3 from the MnO_2 layer and 3 from interlayer water molecules, forming an octahedron. Relaxing the ionic positions of this model using the SCAN + rVV10 functional gives an interlayer distance of 7.08 Å, close to the experimental interlayer distance of ~7.2 Å [35]. We generate an active site, denoted as "*" in Table 1 for OH, O and OOH intermediates, by removing the water molecule in the left of the unit cell (black box in Fig. 1 (a)). The structures of the *OH, *O and *OOH intermediates are shown in Fig. 2(b). Surface reactions in the absence of confinement are modeled by increasing the interlayer distance to about 30 Å to model a monolayer system (MonoL).

Table 1
The employed oxygen-evolution reaction mechanism and energetics. * stands for a reaction site of the catalyst.

Step	Chemistry	Limiting potential (eV)
R1	$H_2O + * \rightarrow HO^* + e^- + H^+$	$\Delta G_1 = G_{OH}$
R2	$HO^* \rightarrow O^* + e^- + H^+$	$\Delta G_2 = G_O - G_{OH}$
R3	$H_2O + O^* \rightarrow HOO^* + e^- + H^+$	$\Delta G_3 = G_{OOH} - G_O$
R4	$HOO^* \rightarrow * + O_2 + e^- + H^+$	$\Delta G_4 = 4.92 - G_{OOH}$

The cobalt-pair model (Co-pair) shown in Fig. 1(b) involves two neighboring edge-sharing Co octahedrons. Note an OH connecting the Co pair is used instead of a water molecule. Removing the water molecule in front of the OH generates the corresponding "*" site for OH and O intermediates, while the active site for OOH intermediates involves an additional removal of the left front water molecule in the unit cell (black box in Fig. 1(b)). The structures of the *OH, *O and *OOH intermediates in the Co-pair model are shown in Fig. 2(c). The models (MonoL, InterL and Co-pair) are constructed such that they have an Mn:Co molar ratio of 4:1, similar to the experimental Co concentration [35]. This also disentangles the effect of Co concentration from those of the confinement and local atomic ordering. The study of Co concentration effect on the catalytic performance is interesting, which however is out of the scope of this paper. For details of the electronic structures of the intermediates, refer Table S8 (bandgap) and Fig. S4 (density of states) in supplementary material.

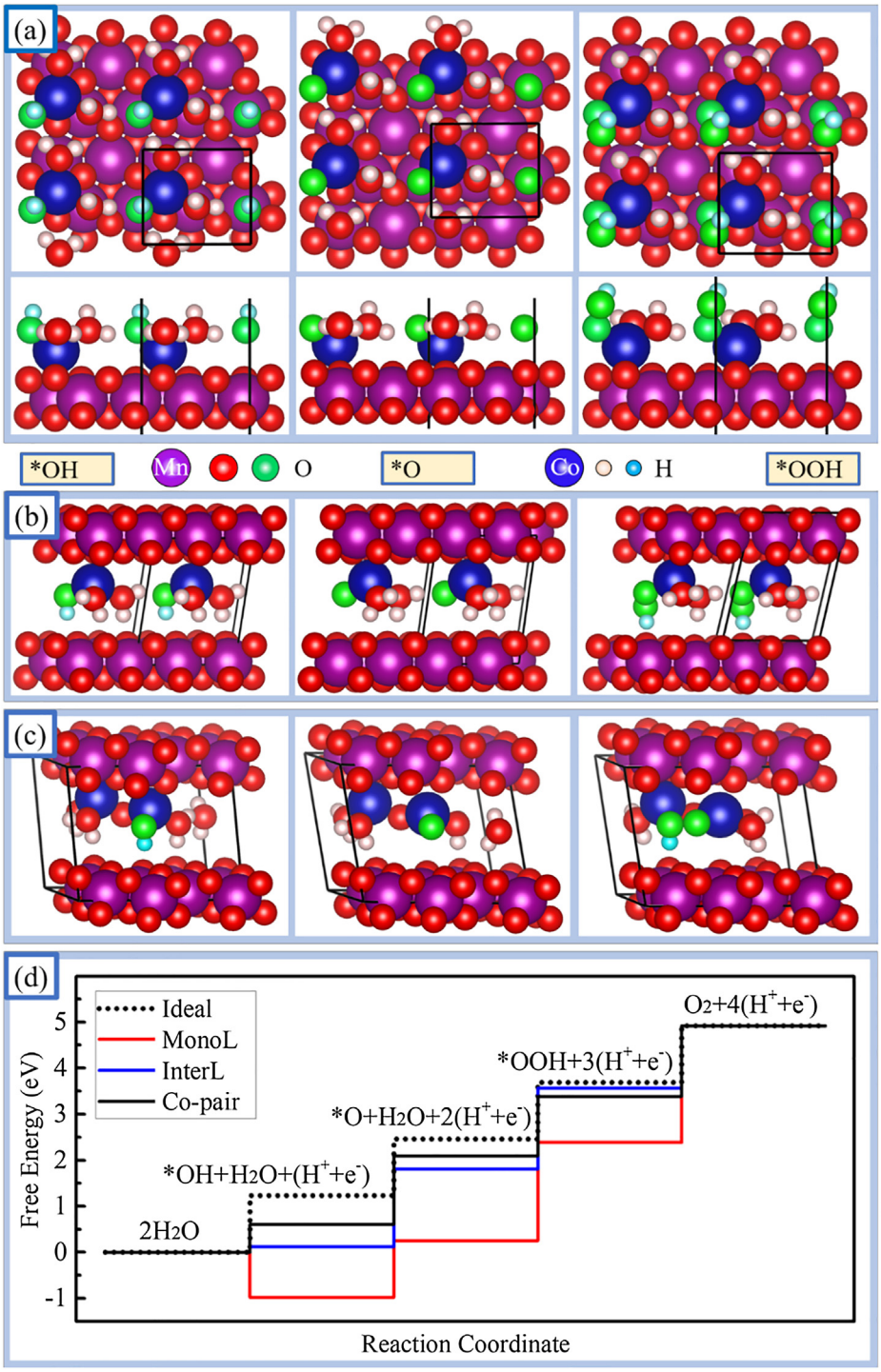

Fig. 2. Relaxed geometries of *OH, *O and *OOH intermediates and calculated OER free energy diagrams of different models revealing the intrinsic atomic interactions in the Co-intercalated layered MnO_2. (a) The Co-decorated MnO_2 monolayer model (MonoL) with both top view (upper panel) and side view (bottom panel), (b) the Co-intercalated layered MnO_2 model with well separated Co-Co distances (InterL), (c) the Co-pair model (Co-pair) where the nearest Co atoms form Co pairs. Oxygen and hydrogen of reaction intermediates are highlighted green and cyan, respectively. Spectator atoms are identified as H (white), O (red), Co (blue), and Mn (purple). The black boxes indicate the unit cell size used for calculations. The vacuum space of the MonoL model is omitted in the plot for simplicity. (d) Calculated OER free energy diagrams of the MonoL model (red), the InterL model (blue), and the Co-pair model (black). The theoretical ideal path is included for reference (dotted, black).

Our model of aqueous birnessite remains a simplified system, and a more detailed model would include Co adsorbates on both sides of each MnO_2 layer. We adopt the simplified single-side Co adsorbate model here because it significantly reduces the computational cost of the calculations, while still presenting a reasonably good model for investigations of the interlayer distance dependence of the adsorption energy and OER overpotential, where the monolayer case is approached at large interlayer distance. The single-side adsorbate model omits interactions between intermediates adsorbed on Co atoms of neighboring MnO_2 layers, which

may also play an active role in enhancing catalytic performance by stabilizing OOH over OH intermediates. However, a study of these effects is beyond the scope of this work.

Detailed structural information (lattice constants, angles, and interlayer distances, and bonding geometries) can be found in Tables S5–S7, and POSCAR files in supplementary materials. Note that Co has a general +2 oxidation state, while Mn have +3 or +4 oxidation states, see Table S9 of supplementary materials.

2.3. Thermodynamics for water oxidation

The water splitting reaction is endothermic with an unfavorable 4.92 eV change in Gibbs free energy. With an ideal catalyst the Gibbs free energy diagram for the elementary reaction steps would be evenly spaced, as shown in Fig. 2(d), requiring an external potential of 4.92 eV/4e = 1.23 V to make each step spontaneous. In reality however, even the catalyzed reaction has an unevenly spaced Gibbs free energy diagram, requiring a larger potential than the ideal 1.23 V for some reaction steps. The theoretical overpotential is defined as the lowest excess potential at which all reaction steps are thermodynamically downhill and is given by the equation:

$$\eta_{OER} = [\max(G_{OH}, G_O - G_{OH}, G_{OOH} - G_O, 4.92 - G_{OOH}) - 1.23eV]/e,$$

where the Gibbs free energy (G) is related to the electronic energy (E), zero-point energy, and the entropic contribution. The OER was modelled assuming the four-step mechanism described in Table 1.

The computational hydrogen electrode method [37], defined as the energetic gain (or loss) by exchange of water and proton/electron pairs from an implicit solvent, was used to calculate adsorption energies of reaction intermediates and describe intermediate thermodynamics analogous to the reversible hydrogen electrode (RHE). Computational hydrogen electrode calculations remain constant for all pH values. Although the acidic and basic OER pathways are different mechanistically, they are equivalent from a thermodynamic perspective. To model the thermochemistry of the OER, we adopt acidic conditions and follow the reaction scheme (R1-R4) given in Table 1. Surface adsorption energies of intermediates are obtained according to

$$\Delta E_{OH} = E_{*OH} + 0.5E_{H_2} - E_* - E_{H_2O}$$

$$\Delta E_O = E_{*O} + E_{H_2} - E_* - E_{H_2O}$$

$$\Delta E_{OOH} = E_{*OOH} + 1.5E_{H_2} - E_* - 2E_{H_2O}$$

The Gibbs free energies of *O, *OH, and *OOH (G_O, G_{OH}, and G_{OOH}) defined in Table 1 are obtained by adding the zero-point energy and entropic corrections to the respective adsorption energies (ΔE_O, ΔE_{OH}, and ΔE_{OOH}), as described in Ref. [37]. The Gibbs free energy of the full reaction was fixed to the experimentally measured value of 4.92 eV [68]. The adsorption energies are presented in Table 2.

Zero-point energies (ZPE) were calculated from vibrational frequencies using finite differences and the selective dynamics method, allowing for displacements of only atoms of the intermediate OH, O and OOH. Our calculated ZPE values presented in Tables S2 and S3 are close to those of a similar system studied by Nørskov and coworkers [69].

3. Results and discussion

In comparison to the theoretical ideal catalyst, Fig. 2 shows that the Co-decorated MnO_2 monolayer (red, the *MonoL* model) overstabilizes the bound intermediates *OH, *O, and *OOH. In contrast, the spatial confinement provided by the interlayer region of Co-intercalated MnO_2 significantly destabilizes these intermediates (blue, the *InterL* model), consistent with previous studies of layered systems [55,70]. Confinement reduces the overpotential from 1.30 V of the Co-decorated MnO_2 monolayer to 0.53 V. The origin of this beneficial destabilization is reflected by the geometric changes of the intermediates due to confinement, highlighted by *OOH that is adsorbed on one sheet, but repelled by oxygen atoms in the opposing MnO_2 layer (i.e., the non-adsorbing side), as shown in Fig. 2(b).

Table 2
Calculated adsorption energies (in units of eV) of the *OH, *O and *OOH OER intermediates within the MonoL, InterL, and Co-pair models.

Intermediates	Co-pair	InterL	MonoL
OH	0.18	−0.31	−1.38
O	2.06	1.77	0.22
OOH	2.90	3.09	1.94

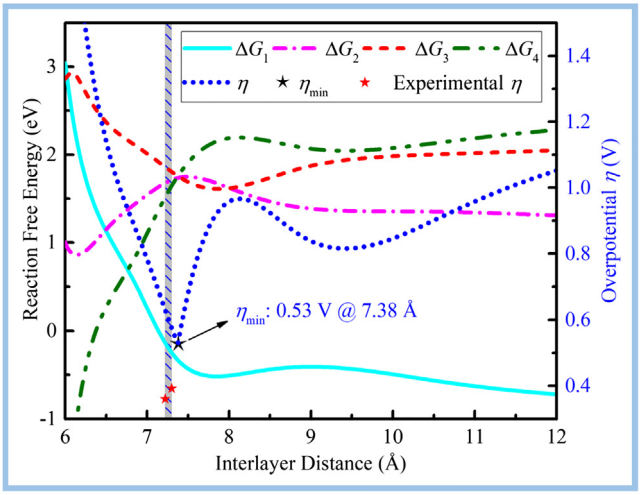

Fig. 3. Calculated interlayer-distance-dependence of the reaction free energies of (R1-R4) and overpotential of OER (dotted) for the Co-intercalated MnO_2. Interlayer distance is taken as the vertical distance of neighboring Mn atomic layers. Detailed structural information for bonding evolution can be found in Fig. S1 in supplementary materials.

The monolayer case can be regarded as a layered MnO_2 in the limit of an infinite interlayer distance. Therefore, it is reasonable to expect that there exists an optimal interlayer distance that minimizes the overpotential, given that the intermediates are overstabilized by the monolayer and destabilized by confinement. Fig. 3 shows the OER reaction free energies of elementary steps and overpotential as functions of the interlayer distance. An optimal distance is identified at 7.38 Å, with an overpotential of 0.53 V, such that confinement reduces the overpotential by 0.77 V in comparison to the monolayer extreme and essentially the same as that of the Co-intercalated layered MnO_2 calculated at equilibrium (the InterL model of Fig. 2(d)). Our result is consistent with a theoretical study on confinement effects in RuO_2 layered materials of Ref. [55], which predicted a similar 0.3 V reduction in overpotential for the OER through confinement effects.

The optimal distance is close to the equilibrium distances of 7.2 to 7.5 Å predicted for different intermediates (see the supplementary materials) and is also consistent with experimental results (~7.2 Å) [35], indicated by the shaded area in Fig. 3. As the layered MnO_2 is compressed, the rate-determining ΔG_3 from *O to *OOH increases dramatically because *OOH is destabilized significantly

more than *O. On the contrary, when the interlayer distance is expanded from the experimental equilibrium distance, *OOH is stabilized more than *O, resulting in a smaller ΔG_3 and a lower overpotential. As the interlayer distance increases further from the optimal distance of 7.38 Å, *OOH becomes too stable and the formation of O_2 in step 4 becomes the rate-determining step, leading to an increase in the overpotential for the OER. Step 4 remains rate-determining for interlayer distances larger than the optimal one, consistent with the monolayer extreme where step 4 is rate-determining.

One interesting feature in the overpotential curve is the second minimum appearing at the interlayer distance around 8.5 Å, reflecting a destabilization mechanism for the OOH intermediate that is the only relevant one for ΔG_4. The destabilization is likely due to breakage of the hydrogen bond between OOH and the opposing MnO_2 layer (see the supplementary materials for the hydrogen bonding analysis), whose competition with the stabilization due to the larger interlayer distance results in the second minimum in the overpotential. The calculated change in overpotential with respect to the interlayer distance for the Co-intercalated layered MnO_2 shown in Fig. 3 is consistent with experimental observations for alkali metal-intercalated layered MnO_2, whose catalytic performance depends on the interlayer distance as tuned by the ionic radius of intercalated cations [71]. It was found experimentally [71] that Cs^+/bilayer MnO_2, with an equilibrium interlayer distance around 11 Å and an overpotential of 0.47 V, has better catalytic performance than K^+/bilayer MnO_2, whose equilibrium interlayer distance was about 7 Å and an overpotential 0.21 V higher than the Cs^+ system. For these experimental results, the second minimum in overpotential of Fig. 3 might be more relevant, but a detailed study of this is beyond the scope of this work.

Confinement effects alone cannot explain the performance of Co-intercalated layered MnO_2 for OER, because the excellent catalytic activity is experimentally observed at an interlayer distance of ~7.2 Å with an overpotential of 0.36 V, much lower than the optimal 0.53 V of Fig. 3. There likely exists a different mechanism that can selectively stabilize one intermediate over the others. As *OOH contains an additional O atom compared to *O, it is natural to expect that *OOH can be further stabilized by forming bonds with the catalyst from both its O atoms. Therefore, we propose a strategy for the selective stabilization of *OOH: the formation of cobalt pairs (termed the *Co-pair* model).

In the *Co-pair* model, each Co atom in the pair interacts with one O atom of an OOH intermediate. The bond length of the Co pair is ~3.3 Å, to be compared with ~5.0 Å between two nearest Co atoms in the InterL model, as illustrated in Fig. 2. The O-O bond length of *OOH intermediate in the Co-pair model is 1.51 Å, almost the same as that in the monolayer surface model (1.50 Å) and slightly larger than that in the interlayer model (1.47 Å). See Table S6 of supplementary material. The *Co-pair* model follows a similar mechanism to the COOH selective stabilization proposed in Ref. [72], and can also be considered as a special case of the promotor mechanism for OOH stabilization described in Ref. [46]. Moreover, two-metal-ion catalysis is a common motif in enzymatic processing of DNA and RNA [73], and our model suggests a generalization of this functional arrangement of ions to non-biological systems. As shown in Fig. 2(d), compared to the InterL model, the *Co-pair* model stabilizes *OOH as expected while destabilizing *O and *OH, resulting in an overpotential of 0.30 V that is in excellent agreement with the experimentally determined 0.36 V [35]. The destabilization of *O and *OH is due to smaller interlayer distances (~7.15 Å) in the *Co-pair* model than in the InterL model (7.2 to 7.5 Å), consistent with the confinement effect found in Fig. 3. We therefore attribute the experimentally found improvement of layered MnO_2 catalytic behavior by Co intercalation to a synergy between confinement effects and local atomic ordering. When we expand the interlayer distance of the *Co-pair* model to essentially create a surface model with Co pairs and thus remove the confinement effect, the intermediates are all overstabilized, resulting in a high overpotential (~1.0 V), comparable to 1.30 V of the *MonoL* model (See Fig. S3 of supplementary material). We note that reactivity may also be altered through enhanced thermal fluctuations of water molecules near the Co pair [36,74], relative to the InterL model, but such fluctuations are ignored in our calculations. It is also noteworthy that the current proposed *Co-pair* model is only one example of many possible transient or metastable intercalant ordering configurations for selective stabilization of *OOH, the only requirement being an ability to coordinate a double Co-O bonding pattern. It is also possible that Co atoms form substitution defects and alter the electronic structure of MnO_2, and hence its catalytic performance [75].The detailed mechanism for the catalytic activity of the Co substituted birnessite, and its interplay with the Co intercalation, remains an open question, and we may examine them in future work.

4. Conclusions

In summary, by analyzing the elementary reaction steps of water oxidation in Co-intercalated layered MnO_2, we reveal that the underlying atomic interactions in the interlayer region of intercalated layered materials can create versatility and lead to catalytic improvements. We also highlight the idea of synergistically using multiple selective (de)stabilization mechanisms for catalyst design and tunability of catalytic performance. This understanding explains several experimental observations and has the potential to accelerate the design of novel non-toxic precious-metal-free catalysts through interlayer engineering of layered materials.

Acknowledgments

We thank Hoang Tran, Carl Baribault, and Hideki Fujioka for their computational support at Tulane University; Funding: This work was supported as part of the Center for Complex Materials from First Principles (CCM), an Energy Frontier Research Center funded by the U.S. Department of Energy, Office of Science, Basic Energy Sciences under Award (DE-SC0012575). Computational resources were provided by the Cypress Computational Cluster at Tulane University and the EFRC cluster at Temple University.

Appendix A. Supplementary material

Supplementary data to this article can be found online at https://doi.org/10.1016/j.jcat.2019.04.037.

References

[1] N.S. Lewis, D.G. Nocera, Powering the planet: Chemical challenges in solar energy utilization, Proc. Natl. Acad. Sci. 103 (2006) 15729–15735.
[2] C.C. McCrory, S. Jung, J.C. Peters, T.F. Jaramillo, Benchmarking heterogeneous electrocatalysts for the oxygen evolution reaction, J. Am. Chem. Soc. 135 (2013) 16977–16987.
[3] D.G. Nocera, The artificial leaf, Acc. Chem. Res. 45 (2012) 767–776.
[4] M.G. Walter, E.L. Warren, J.R. McKone, S.W. Boettcher, Q. Mi, E.A. Santori, N.S. Lewis, Solar water splitting cells, Chem. Rev. 110 (2010) 6446–6473.
[5] T.A. Betley, Q. Wu, T. Van Voorhis, D.G. Nocera, Electronic design criteria for O–O bond formation via metal– oxo complexes, Inorg. Chem. 47 (2008) 1849–1861.
[6] T.R. Cook, D.K. Dogutan, S.Y. Reece, Y. Surendranath, T.S. Teets, D.G. Nocera, Solar energy supply and storage for the legacy and nonlegacy worlds, Chem. Rev. 110 (2010) 6474–6502.
[7] Y. Lee, J. Suntivich, K.J. May, E.E. Perry, Y. Shao-Horn, Synthesis and activities of rutile IrO2 and RuO2 nanoparticles for oxygen evolution in acid and alkaline solutions, J. Phys. Chem. Lett. 3 (2012) 399–404.
[8] Y. Gorlin, T.F. Jaramillo, A bifunctional nonprecious metal catalyst for oxygen reduction and water oxidation, J. Am. Chem. Soc. 132 (2010) 13612–13614.

[9] R. Subbaraman, D. Tripkovic, K.-C. Chang, D. Strmcnik, A.P. Paulikas, P. Hirunsit, M. Chan, J. Greeley, V. Stamenkovic, N.M. Markovic, Trends in activity for the water electrolyser reactions on 3d M (Ni Co, Fe, Mn) hydr (oxy) oxide catalysts, Nat. Mater. 11 (2012) 550.
[10] M.S. Burke, M.G. Kast, L. Trotochaud, A.M. Smith, S.W. Boettcher, Cobalt–iron (oxy) hydroxide oxygen evolution electrocatalysts: the role of structure and composition on activity, stability, and mechanism, J. Am. Chem. Soc. 137 (2015) 3638–3648.
[11] B. Zhang, X. Zheng, O. Voznyy, R. Comin, M. Bajdich, M. García-Melchor, L. Han, J. Xu, M. Liu, L. Zheng, Homogeneously dispersed multimetal oxygen-evolving catalysts, Science 352 (2016) 333–337.
[12] M. Gong, Y. Li, H. Wang, Y. Liang, J.Z. Wu, J. Zhou, J. Wang, T. Regier, F. Wei, H. Dai, An advanced Ni–Fe layered double hydroxide electrocatalyst for water oxidation, J. Am. Chem. Soc. 135 (2013) 8452–8455.
[13] Y. Elbaz, M. Caspary Toroker, Dual mechanisms: hydrogen transfer during water oxidation catalysis of pure and Fe-doped nickel oxyhydroxide, J. Phys. Chem. C 121 (2017) 16819–16824.
[14] A.J. Tkalych, H.L. Zhuang, E.A. Carter, A density functional+ U assessment of oxygen evolution reaction mechanisms on β-NiOOH, ACS Catal. 7 (2017) 5329–5339.
[15] Y.-F. Li, A. Selloni, Mechanism and activity of water oxidation on selected surfaces of pure and Fe-doped NiOx, Acs Catal. 4 (2014) 1148–1153.
[16] C. Tang, N. Cheng, Z. Pu, W. Xing, X. Sun, NiSe nanowire film supported on nickel foam: an efficient and stable 3D bifunctional electrode for full water splitting, Angewandte Chemie 127 (2015) 9483–9487.
[17] Q. Liu, J. Jin, J. Zhang, NiCo2S4@ graphene as a bifunctional electrocatalyst for oxygen reduction and evolution reactions, ACS Appl. Mater. Interfaces 5 (2013) 5002–5008.
[18] M.-R. Gao, Y.-F. Xu, J. Jiang, S.-H. Yu, Nanostructured metal chalcogenides: synthesis, modification, and applications in energy conversion and storage devices, Chem. Soc. Rev. 42 (2013) 2986–3017.
[19] M.W. Kanan, D.G. Nocera, In situ formation of an oxygen-evolving catalyst in neutral water containing phosphate and Co^{2+}, Science 321 (2008) 1072–1075.
[20] M.W. Kanan, Y. Surendranath, D.G. Nocera, Cobalt–phosphate oxygen-evolving compound, Chem. Soc. Rev. 38 (2009) 109–114.
[21] Y. Surendranath, M.W. Kanan, D.G. Nocera, Mechanistic studies of the oxygen evolution reaction by a cobalt-phosphate catalyst at neutral pH, J. Am. Chem. Soc. 132 (2010) 16501–16509.
[22] P. Du, R. Eisenberg, Catalysts made of earth-abundant elements (Co, Ni, Fe) for water splitting: recent progress and future challenges, Energy Environ. Sci. 5 (2012) 6012–6021.
[23] J. Suntivich, K.J. May, H.A. Gasteiger, J.B. Goodenough, Y. Shao-Horn, A perovskite oxide optimized for oxygen evolution catalysis from molecular orbital principles, Science 334 (2011) 1383–1385.
[24] B. Lanson, V.A. Drits, Q. Feng, A. Manceau, Structure of synthetic Na-birnessite: Evidence for a triclinic one-layer unit cell, Am. Mineral. 87 (2002) 1662–1671.
[25] J.E. Post, D.R. Veblen, Crystal structure determinations of synthetic sodium, magnesium, and potassium birnessite using TEM and the Rietveld method, Am. Mineral. 75 (1990) 477–489.
[26] V.A. Drits, E. Silvester, A.I. Gorshkov, A. Manceau, Structure of synthetic monoclinic Na-rich birnessite and hexagonal birnessite: I. Results from X-ray diffraction and selected-area electron diffraction, Am. Mineral. 82 (1997) 946–961.
[27] D. Golden, J. Dixon, C. Chen, Ion exchange, thermal transformations, and oxidizing properties of birnessite, Clays Clay Miner. 34 (1986) 511–520.
[28] J. Yano, J. Kern, K. Sauer, M.J. Latimer, Y. Pushkar, J. Biesiadka, B. Loll, W. Saenger, J. Messinger, A. Zouni, Where water is oxidized to dioxygen: structure of the photosynthetic Mn4Ca cluster, Science 314 (2006) 821–825.
[29] A. Guskov, J. Kern, A. Gabdulkhakov, M. Broser, A. Zouni, W. Saenger, Cyanobacterial photosystem II at 2.9-Å resolution and the role of quinones, lipids, channels and chloride, Nat. Struct. Mol. Biol. 16 (2009) 334.
[30] J. Barber, Photosynthetic energy conversion: natural and artificial, Chem. Soc. Rev. 38 (2009) 185–196.
[31] Y. Meng, W. Song, H. Huang, Z. Ren, S.-Y. Chen, S.L. Suib, Structure–property relationship of bifunctional MnO_2 nanostructures: highly efficient, ultra-stable electrochemical water oxidation and oxygen reduction reaction catalysts identified in alkaline media, J. Am. Chem. Soc. 136 (2014) 11452–11464.
[32] A.C. Thenuwara, S.L. Shumlas, N.H. Attanayake, E.B. Cerkez, I.G. McKendry, L. Frazer, E. Borguet, Q. Kang, M.J. Zdilla, J. Sun, Copper-intercalated birnessite as a water oxidation catalyst, Langmuir 31 (2015) 12807–12813.
[33] M. Nakayama, Y. Fujii, K. Fujimoto, M. Yoshimoto, A. Kaide, T. Saeki, H. Asada, Electrochemical synthesis of a nanohybrid film consisting of stacked graphene sheets and manganese oxide as oxygen evolution reaction catalyst, RSC Adv. 6 (2016) 23377–23382.
[34] R. Pokhrel, M.K. Goetz, S.E. Shaner, X. Wu, S.S. Stahl, The "best catalyst" for water oxidation depends on the oxidation method employed: a case study of manganese oxides, J. Am. Chem. Soc. 137 (2015) 8384–8387.
[35] A.C. Thenuwara, S.L. Shumlas, N.H. Attanayake, Y.V. Aulin, I.G. McKendry, Q. Qiao, Y. Zhu, E. Borguet, M.J. Zdilla, D.R. Strongin, Intercalation of cobalt into the interlayer of birnessite improves oxygen evolution catalysis, ACS Catal. 6 (2016) 7739–7743.
[36] A.C. Thenuwara, E.B. Cerkez, S.L. Shumlas, N.H. Attanayake, I.G. McKendry, L. Frazer, E. Borguet, Q. Kang, R.C. Remsing, M.L. Klein, Nickel confined in the interlayer region of birnessite: an active electrocatalyst for water oxidation, Angew. Chemie Int. Ed. 55 (2016) 10381–10385.
[37] J.K. Nørskov, J. Rossmeisl, A. Logadottir, L. Lindqvist, J.R. Kitchin, T. Bligaard, H. Jonsson, Origin of the overpotential for oxygen reduction at a fuel-cell cathode, J. Phys. Chem. B 108 (2004) 17886–17892.
[38] J.K. Nørskov, T. Bligaard, J. Rossmeisl, C.H. Christensen, Towards the computational design of solid catalysts, Nat. Chem. 1 (2009) 37.
[39] F. Abild-Pedersen, J. Greeley, F. Studt, J. Rossmeisl, T. Munter, P.G. Moses, E. Skulason, T. Bligaard, J.K. Nørskov, Scaling properties of adsorption energies for hydrogen-containing molecules on transition-metal surfaces, Phys. Rev. Lett. 99 (2007) 016105.
[40] J.K. Nørskov, T. Bligaard, A. Logadottir, S. Bahn, L.B. Hansen, M. Bollinger, H. Bengaard, B. Hammer, Z. Sljivancanin, M. Mavrikakis, Universality in heterogeneous catalysis, J. Catal. 209 (2002) 275–278.
[41] J. Rossmeisl, A. Logadottir, J.K. Nørskov, Electrolysis of water on (oxidized) metal surfaces, Chem. Phys. 319 (2005) 178–184.
[42] A. Valdes, J. Brillet, M. Grätzel, H. Gudmundsdottir, H.A. Hansen, H. Jonsson, P. Klüpfel, G.-J. Kroes, F. Le Formal, I.C. Man, Solar hydrogen production with semiconductor metal oxides: new directions in experiment and theory, PCCP 14 (2012) 49–70.
[43] F. Calle-Vallejo, J. Martínez, J.M. García-Lastra, J. Rossmeisl, M. Koper, Physical and chemical nature of the scaling relations between adsorption energies of atoms on metal surfaces, Phys. Rev. Lett. 108 (2012) 116103.
[44] E. Shustorovich, Chemisorption phenomena: Analytic modeling based on perturbation theory and bond-order conservation, Surf. Sci. Rep. 6 (1986) 1–63.
[45] F. Calle-Vallejo, N.G. Inoglu, H.-Y. Su, J.I. Martínez, I.C. Man, M.T. Koper, J.R. Kitchin, J. Rossmeisl, Number of outer electrons as descriptor for adsorption processes on transition metals and their oxides, Chem. Sci. 4 (2013) 1245–1249.
[46] J.H. Montoya, L.C. Seitz, P. Chakthranont, A. Vojvodic, T.F. Jaramillo, J.K. Nørskov, Materials for solar fuels and chemicals, Nat. Mater. 16 (2017) 70.
[47] N.B. Halck, V. Petrykin, P. Krtil, J. Rossmeisl, Beyond the volcano limitations in electrocatalysis–oxygen evolution reaction, PCCP 16 (2014) 13682–13688.
[48] K. Chan, C. Tsai, H.A. Hansen, J.K. Nørskov, Molybdenum sulfides and selenides as possible electrocatalysts for CO2 reduction, ChemCatChem 6 (2014) 1899–1905.
[49] B.A. Rosen, A. Salehi-Khojin, M.R. Thorson, W. Zhu, D.T. Whipple, P.J. Kenis, R.I. Masel, Ionic liquid–mediated selective conversion of CO_2 to CO at low overpotentials, Science 334 (2011) 643–644.
[50] M.R. Thorson, K.I. Siil, P.J. Kenis, Effect of cations on the electrochemical conversion of CO_2 to CO, J. Electrochem. Soc. 160 (2013) F69–F74.
[51] L. Sun, G.K. Ramesha, P.V. Kamat, J.F. Brennecke, Switching the reaction course of electrochemical CO_2 reduction with ionic liquids, Langmuir 30 (2014) 6302–6308.
[52] C.W. Li, J. Ciston, M.W. Kanan, Electroreduction of carbon monoxide to liquid fuel on oxide-derived nanocrystalline copper, Nature 508 (2014) 504.
[53] X. Feng, K. Jiang, S. Fan, M.W. Kanan, Grain-boundary-dependent CO_2 electroreduction activity, J. Am. Chem. Soc. 137 (2015) 4606–4609.
[54] Y. Chen, C.W. Li, M.W. Kanan, Aqueous CO_2 reduction at very low overpotential on oxide-derived Au nanoparticles, J. Am. Chem. Soc. 134 (2012) 19969–19972.
[55] A.D. Doyle, J.H. Montoya, A. Vojvodic, Improving oxygen electrochemistry through nanoscopic confinement, ChemCatChem 7 (2015) 738–742.
[56] W. Kohn, L.J. Sham, Self-consistent equations including exchange and correlation effects, Phys. Rev. 140 (1965) A1133.
[57] G. Kresse, J. Furthmüller, Efficient iterative schemes for ab initio total-energy calculations using a plane-wave basis set, Phys. Rev. B 54 (1996) 11169.
[58] P.E. Blöchl, Projector augmented-wave method, Phys. Rev. B 50 (1994) 17953.
[59] G. Kresse, D. Joubert, From ultrasoft pseudopotentials to the projector augmented-wave method, Phys. Rev. B 59 (1999) 1758.
[60] J. Sun, R.C. Remsing, Y. Zhang, Z. Sun, A. Ruzsinszky, H. Peng, Z. Yang, A. Paul, U. Waghmare, X. Wu, Accurate first-principles structures and energies of diversely bonded systems from an efficient density functional, Nat. Chem. 8 (2016) 831.
[61] J. Sun, A. Ruzsinszky, J.P. Perdew, Strongly constrained and appropriately normed semilocal density functional, Phys. Rev. Lett. 115 (2015) 036402.
[62] J. Sun, B. Xiao, Y. Fang, R. Haunschild, P. Hao, A. Ruzsinszky, G.I. Csonka, G.E. Scuseria, J.P. Perdew, Density functionals that recognize covalent, metallic, and weak bonds, Phys. Rev. Lett. 111 (2013) 106401.
[63] D.A. Kitchaev, H. Peng, Y. Liu, J. Sun, J.P. Perdew, G. Ceder, Energetics of MnO_2 polymorphs in density functional theory, Phys. Rev. B 93 (2016) 045132.
[64] H. Peng, J.P. Perdew, Synergy of van der Waals and self-interaction corrections in transition metal monoxides, Phys. Rev. B 96 (2017) 100101.
[65] J.W. Furness, Y. Zhang, C. Lane, I.G. Buda, B. Barbiellini, R.S. Markiewicz, A. Bansil, J. Sun, An accurate first-principles treatment of doping-dependent electronic structure of high-temperature cuprate superconductors, Commun. Phys. 1 (2018) 11.
[66] R. Sabatini, T. Gorni, S. de Gironcoli, Nonlocal van der Waals density functional made simple and efficient, Phys. Rev. B 87 (2013) 041108.
[67] O.A. Vydrov, T. Van Voorhis, Nonlocal van der Waals density functional: The simpler the better, J. Chem. Phys. 133 (2010) 244103.
[68] M.H. William, D. Lide, T. Bruno, CRC handbook of chemistry and physics, CRC Press, Boca Raton, FL USA, 2011.
[69] M. Bajdich, M. García-Mota, A. Vojvodic, J.K. Nørskov, A.T. Bell, Theoretical investigation of the activity of cobalt oxides for the electrochemical oxidation of water, J. Am. Chem. Soc. 135 (2013) 13521–13530.

[70] H. Li, J. Xiao, Q. Fu, X. Bao, Confined catalysis under two-dimensional materials, Proc. Natl. Acad. Sci. (2017) 201701280.
[71] Q. Kang, L. Vernisse, R.C. Remsing, A.C. Thenuwara, S.L. Shumlas, I.G. McKendry, M.L. Klein, E. Borguet, M.J. Zdilla, D.R. Strongin, Effect of interlayer spacing on the activity of layered manganese oxide bilayer catalysts for the oxygen evolution reaction, J. Am. Chem. Soc. 139 (2017) 1863–1870.
[72] H.A. Hansen, J.B. Varley, A.A. Peterson, J.K. Nørskov, Understanding trends in the electrocatalytic activity of metals and enzymes for CO_2 reduction to CO, J. Phys. Chem. Lett. 4 (2013) 388–392.
[73] G. Palermo, A. Cavalli, M.L. Klein, M. Alfonso-Prieto, M. Dal Peraro, M. De Vivo, Catalytic metal ions and enzymatic processing of DNA and RNA, Acc. Chem. Res. 48 (2015) 220–228.
[74] R.C. Remsing, I.G. McKendry, D.R. Strongin, M.L. Klein, M.J. Zdilla, Frustrated solvation structures can enhance electron transfer rates, J. Phys. Chem. Lett. 6 (2015) 4804–4808.
[75] I.G. McKendry, L.J. Mohamad, A.C. Thenuwara, T. Marshall, E. Borguet, D.R. Strongin, M.J. Zdilla, Synergistic in-layer cobalt doping and interlayer iron intercalation into layered MnO_2 produces an efficient water oxidation electrocatalyst, ACS Energy Lett. 3 (2018) 2280–2285.